Oral presentation | Turbulent flow

Turbulent flow-II

Wed. Jul 17, 2024 10:45 AM - 12:45 PM Room B

[7-B-04] Comparison of ILES and RANS Computation of Subsonic Base Flow over Axisymmetric Body

*Jaehyoung Park[1], Donguk Kim[1], Seungsoo Lee[1], Jin Seok Park[1] (1. Departmant of Aerospace Engineering, Inha University)

Keywords: base flow, flow separation, turbulent flow, large eddy simulation, RASN

Twelfth International Conference on Computational Fluid Dynamics (ICCFD12), Kobe, Japan, July 14-19, 2024

ICCFD12-2024-xxxx

Comparison and Analysis of Between ILES and RANS Results for Turbulent Base Flow Over an Axisymmetric Body

Jaehyoung Park[*], Donguk Kim[*], Seungsoo Lee[*], Jin Seok Park[*]
Corresponding author: jinseok.park@inha.ac.kr
* Department of Aerospace Engineering, Inha University, Korea

Abstract: In this study, we conducted numerical simulations of subsonic flow over an axisymmetric blunt-based body using two turbulence modeling approaches: implicit large eddy simulations (ILES) with a high-order flux reconstruction scheme, and Reynolds-averaged Navier-Stokes (RANS) simulations with a second-order finite volume method. The simulations were compared with previous experimental results in terms of base pressure, recirculation length, and velocity profiles. It was found that ILES effectively resolve the unsteady flow evolution of small-scale vortical structures, providing better predictions of base pressure. Notably, the base pressure coefficient obtained from fifth-order ILES showed superior agreement with experimental data. The mean flow structure and turbulent characteristics around the recirculation region were also examined and compared.

Keywords: base flow, Turbulent flow, Implicit Large Eddy Simulation, RANS Turbulence model

1 Introduction

It is well-known that base drag constitutes a significant portion of the overall drag acting on an object. Therefore, in order to accurately predict base drag, it is necessary to predict the base pressure accurately. However, it is widely recognized that measuring and predicting the flow around the base can be quite challenging. In wind tunnel experiments, additional structures such as supports or stings are often added to the test object due to the need for fix or mounting. Consequently, when measuring the flow characteristics of the base flow located downstream of these structures, interference caused by the existence of the support structures can't be avoided and becomes part of the observed flow characteristics. In addition, due to practical considerations such as computational cost, computational fluid dynamics (CFD) simulations often depend on the use of Reynolds-Averaged Navier-Stokes (RANS) turbulence models for most real-world problems.

The advantage of Reynolds Averaged Navier Stokes (RANS) turbulence models for general turbulence problems is that they are simulated to find a steady state solution, so the computational cost is reasonable. On the other hand, RANS turbulence models are modelled based on an attached boundary layer, so RANS turbulence models can provide sufficient numerical accuracy in problems with an attached boundary layer. However, in the near wake region around the base, the RANS turbulence model is very inaccurate.

In order to accurately simulate the base near wake region, it is necessary to perform large-scale unsteady turbulence simulations at the level of Large Eddy Simulation (LES). Therefore, there are studies to improve the results of simulations using the RANS turbulence model. One of these studies is our previous work [1]. In our previous work, we improved the RANS turbulence model by machine learning using base flow experiments and LES results performed by Merz [2], Herrin and Dutton [3], Kawaii et al [4] for the base only model without nose cone. There is also a study [5] that performed wind tunnel experiments and LES on the full projectile geometry including the nose cone. This study was conducted under different geometry and different flow conditions than our study, and in that study, the base drag was studied and it was found that the boundary layer thickness near the base edge, the recirculation size downstream of the base, and the base pressure, which determines the base drag, are closely related to each other.

In this study, we conducted numerical simulations of subsonic flow over an axisymmetric blunt-based body using two turbulence modeling approaches: implicit large eddy simulations (ILES) with a high-order flux reconstruction scheme, and Reynolds-averaged Navier-Stokes (RANS) simulations with a second-order finite volume method. In Section 2, we explain the two simulation methodologies and provide a detailed description of the axisymmetric blunt-based body. In Section 3, simulation results are compared in terms of averaged base pressure, mean flow structure, and turbulent characteristics. Section 4 discusses the relationship between base pressure, the recirculation region, and upstream boundary layer flow. Finally, in Section 5, conclusions are drawn.

2 Simulation Setup

2.1 Overview

In this study, we conducted simulations of turbulent flow over an axisymmetric blunt-based body, previously investigated experimentally and numerically by Marrioti et al. The wind-tunnel experiment featured a $25\ m/s$ free-stream flow striking a baseline model supported above a flat plate by a faired strut [5]. Pressure on the base surface and velocity in the wake region were measured. Variational multi-scale large-eddy simulation (VMS LES) and direct numerical simulations (DNS) at reduced Reynolds numbers were performed and compared with experimental results, focusing on time-averaged pressure coefficient distribution and recirculation region size [5]. We conducted Reynolds-averaged Navier-Stokes (RANS) simulation and implicit large-eddy simulation (ILES), comparing them with experimental data. The model, as shown in Figure 1, comprises a 3:1 elliptic nose and cylindrical body, with a fineness ratio of 5.714. Our simulations excluded the strut support used in the experiment. The Reynolds number (Re_D), based on body diameter D, freestream velocity u_∞, freestream density ρ_∞, and fluid viscosity μ_∞, was set at 9.6×10^4. For computational purposes, the Mach number was set at 0.1.

Figure 1: Model of the axisymmetric blunt-based body, showing the 3:1 elliptic nose and cylindrical afterbody.

2.2 Numerical Methods

2.2.1 Implicit Large Eddy Simulation (ILES)

The implicit large eddy simulations were conducted using PyFR, an open-source Python-based framework for solving the Navier-Stokes equations using the high-order flux reconstruction (FR) approach. Specifically, the compressible Navier-Stokes equations with constant viscosity were solved using PyFR 1.15. For spatial discretization, we employed a discontinuous Galerkin (DG) scheme. Third and fourth-order solution polynomials (nominally fourth and fifth-order accurate in space) were considered, referred to as P3 and P4 schemes, respectively. The solution points within each tetrahedral element were positioned according to Shunn-Ham points [6], while the flux points on each face were located using Williams-Shunn points [7]. We employed Roe's Flux Difference Splitting (FDS) method[8] to compute common inviscid fluxes, and a local discontinuous Galerkin (LDG) approach [9] for common viscous fluxes. Temporal advancement was achieved using an explicit RK45[2R+] scheme [10] coupled with adaptive PI time-step control [11]. We adopted a wall-resolved ILES approach, which eliminated the need for an explicit turbulence model. To mitigate aliasing-driven instabilities arising from collocation-type projection, which are especially significant in high Reynolds number flows, we implemented an anti-aliasing strategy. This approach utilized an approximate L^2 projection combined with an appropriate quadrature rule when mapping non-polynomial volume and surface fluxes. This technique was essential for maintaining numerical stability in our simulations.

Simulations were initiated from a freestream condition at a reduced Reynolds number. The initial phase employed first-order solution polynomials and ran for 150 d/u_∞ time units to facilitate the passing initial transients. Following this warm-up period, the simulation was restarted using the designed order solution polynomials at the target Reynolds number and continued for an additional 750 d/u_∞ time units. Data extraction for time-averaged values occurred during the final 300 d/u_∞ time units, which corresponds to approximately 10 passes over the body. To obtain unsteady flow solutions efficiently, GPU-accelerated computations were performed using the CUDA backend of PyFR on the KISTI Neuron supercomputer, which is equipped with NVIDIA V100 and A100 GPUs .

2.2.2 RANS Simulation

The RANS simulations were conducted using an in-house flow solver, MSAPv, which employs the conventional finite volume method. MSAPv solves the compressible Reynolds-averaged Navier-Stokes equations in two- or three-dimensional space using a multi-block structured grid topology. In this study, axisymmetric flow simulations were computed on a two-dimensional grid, utilizing a source-term to account for flow symmetry in the averaged flow. For spatial discretization, the TVD-MUSCL scheme [12] was used to achieve second-order accuracy. Inviscid fluxes were computed using Roe's FDS, while viscous fluxes were calculated using central differencing. Temporal discretization utilized the AF-ADI scheme [13] to efficiently obtain steady-state solutions. Parallel computations were conducted using the MPI standard on the local CPU cluster to obtain converged solutions efficiently, with pressure residuals reduced by more than three orders of magnitude.

The k-ω SST turbulence model (henceforth referred to as the SST model) was chosen as the baseline turbulence model. Based on previous studies, Ristorcelli's compressibility correction was optimized and implemented to enhance the accuracy of the base flow in subsonic to supersonic regions. The empirical coefficients were tuned using Bayesian optimization to match the base pressure mesaured in experiments for base-alone shapes [1]. In this study, both the original form of the compressibility correction (henceforth referred to as the SST-CC model) and the optimized version (henceforth referred to as the SST-CC-opt model) were also employed.

2.3 Domains and Grids

For the ILES, a three-dimensional domain was considered to resolve the evolution of unsteady turbulent flow features. Quadratically curved tetrahedral elements were generated to represent the axisymmetric blunt-based body. Elements adjacent to the body surface were sized such that the first solution point was at a distance equivalent to $y^+ \approx 1$ from the wall (where y^+ is based on the flat plate boundary layer at Reynolds number 96,000). The ILES grid consisted of 1.2 million tetrahedral elements, resulting in 24 million and 42 million degrees of freedom per equation for the P3 and P4 schemes, respectively.

In contrast, a two-dimensional axisymmetric domain was employed for the RANS simulations, utilizing multi-block structured grid topology. The first element height adjacent to the body was positioned at a distance equivalent to $y^{+}\approx 1$ from the wall. The grid consisted of approximately 30,000 grid points.

The grid and boundary conditions are illustrated in Fig. 2. Riemann-invariant boundary conditions were applied in the far field, and no-slip adiabatic wall boundary conditions were applied on the body surface.

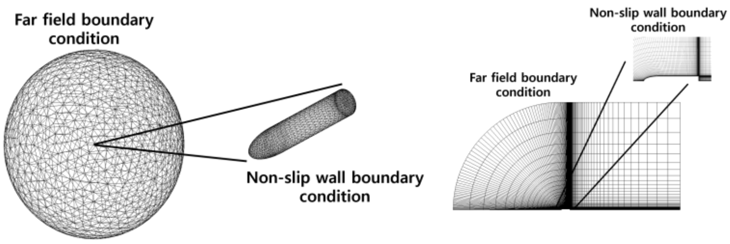

Figure 2: Grids and Boundary conditions ILES(left), RANS(right).

2.4 Post-processing and Flow visualization

The steady RANS simulation results were computed and stored as cell values. This data was represented at each grid point by averaging the values of the cells that shared the point. For the unsteady ILES, the results were computed and stored as solution values at the points within each cell, representing high-order polynomials for each cell. To analyze and visualize the high-order solutions, a very fine multi-block structured grid was created. The high-order solutions were then mapped to each grid point of this fine grid through interpolation. This multi-block grid consisted of approximately 100 million grid points.

The time-averaged (ensemble-averaged) solutions for the ILES were obtained by averaging the unsteady flow field every 2,000 iterations, which is approximately 0.05 non-dimensional time units. Additionally, space-averaged solutions were obtained by converting the three-dimensional flow field from Cartesian coordinates to cylindrical coordinates and averaging along the azimuthal direction. The velocity vector (u, v, w) in three-dimensional domain was converted to the vector (u, v_r, v_θ) in two-dimensional axis-symmetric domain:

$$v_r = v\cos\theta + w\sin\theta$$
$$v_\theta = -v\sin\theta + w\cos\theta$$

where θ is azimuthal angle.

3 Numerical Results

3.1 Base Pressure Distribution

Table 1 compares the base pressure coefficient (C_{pb}), obtained by area-averaging the pressure on the base surface. The experimental results are from Mariotti's study of a smooth surface model. Compared to the experiments, the RANS results showed an error of more than 20%. Unlike previous studies, the compressibility correction overpredicted the base pressure compared to the baseline SST model. However, the ILES results had an error of less than 5%. Notably, the ILES P4 results predicted the base pressure very closely to the experimental results.

Table 1 Comparison of Base Pressure for various schemes

	ILES P3	ILES P4	RANS SST	RANS SST + CC	RANS SST + CC-Opt	Experiment
C_{pb}	-0.154	-0.16	-0.131	-0.128	-0.126	-0.16

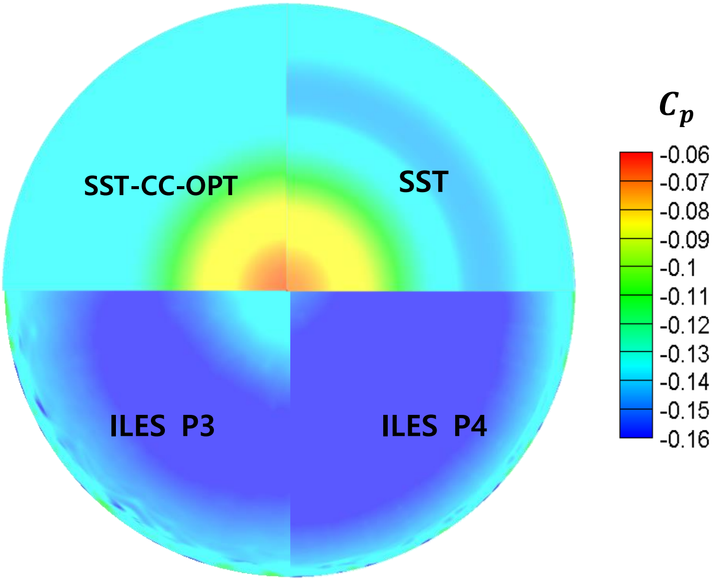

Figure 3: Comparison of time-averaged base pressure contours for various simulations

Figure 3 compares the time-averaged base pressure contours for various schemes. The axisymmetric RANS data was revolved around the symmetry axis to generate a three-dimensional representation. The most distinguishing difference is the pressure distribution around the base center. While the RANS simulation predicts a significant pressure rise at the base center, the pressure distribution for ILES is almost flat, except at the rim of the base.

Figure 4 shows the base pressure distribution along the radial direction. The ILES distribution was obtained by time and space averaging. While a steep pressure gradient near the base center was observed for the RANS simulations, the ILES results do not show such a gradient. Particularly, the ILES P4 results agree well with the experimental distribution.

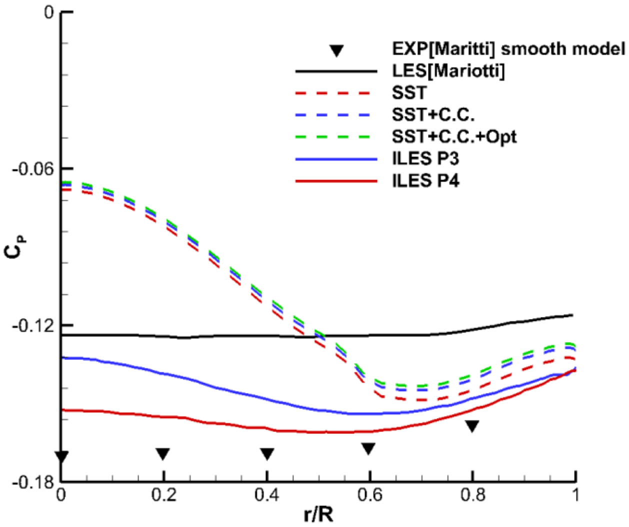

Figure 4: Base pressure distribution along radial direction

3.2 Mean Flow Characteristics in the Recirculation Zone

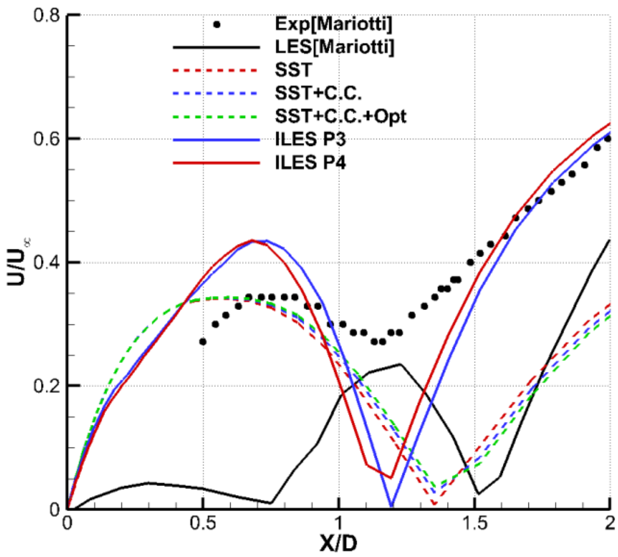

Figure 5: Axial velocity distribution along the centerline, non-dimensionalized by the free-stream velocity

To investigate the variation in base pressure, the flow characteristics downstream of the base, particularly around the recirculation zone, were analyzed. Figure 5 illustrates the axial velocity distribution along the centerline. Compared to RANS results, ILES predicts a shorter recirculation zone with higher mean axial velocities in that region. The position of the recirculation zone observed in the experiment closely matches that predicted by ILES. Figure 6 compares the time- and space- averaged velocity contours around the base surface. It is also confirmed that ILES resolve a shorter recirculation zone. Table 2 compares the recirculation length l_r for the various schemes. ILES predicted shorter length than RANS simulations. for the various schemes. ILES predicted a shorter length than RANS simulations. Although the recirculation length measurement was challenging and had low accuracy, ILES results are close to the experimental findings.

Table 2 Comparison of recirculation size ($\mathbf{l_r}$), non-dimensionalized by the diameter (d)

	ILES P3	ILES P4	RANS SST	RANS SST + CC	RANS SST + CC-Opt	Experiment
l_r/d	1.2	1.15	1.368	1.4	1.42	1.26

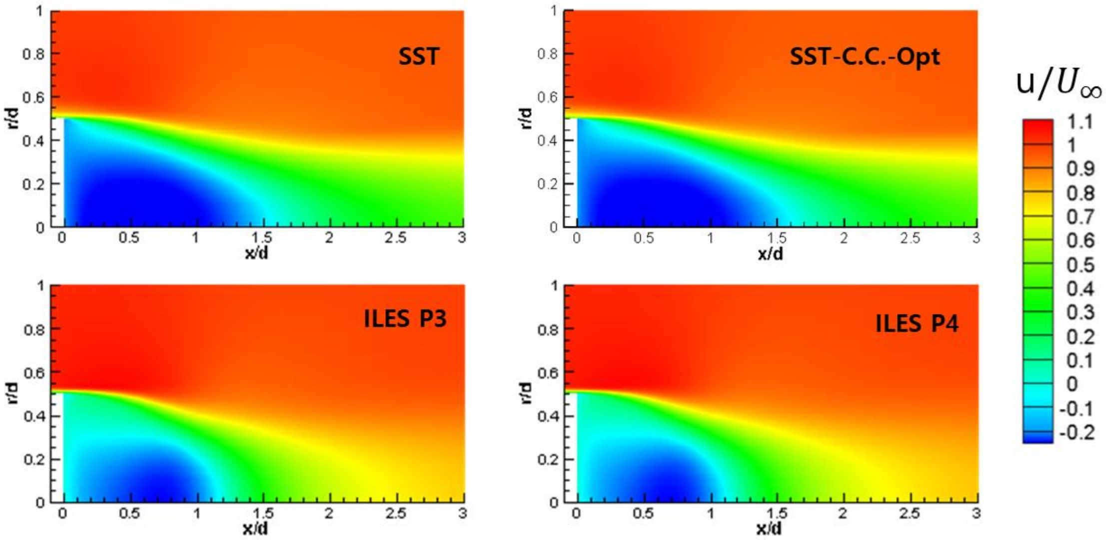

Figure 6: Time and space averaged velocity contour around base

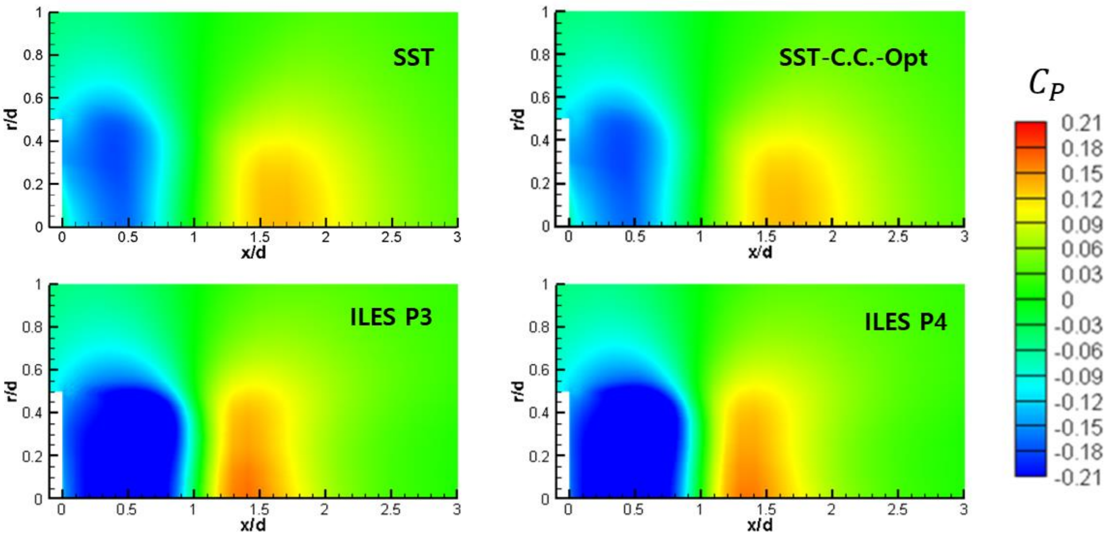

Figure 7: Time and space averaged pressure contour around base

Figure 7 compares the time- and space-averaged pressure contours around the base surface. ILES yields a narrower but lower pressure region around the recirculation zone compared to the RANS results. After the recirculation zone, ILES also develops a narrower higher pressure region. This indicate that the ILES predict stronger vortex around the recirculation zone.

3.3 Turbulent Flow Characteristics

To understand the factors influencing the variation in vortex strength, we analyzed turbulent flow characteristics, such as turbulent kinetic energy (TKE) and Reynolds stress. Figure 8 compares the turbulent kinetic energy k for various methods. ILES results show significantly higher TKE around the recirculation region compared to RANS results. Specifically, ILES P4 exhibits higher TKE in both the recirculation region and near the base wall.

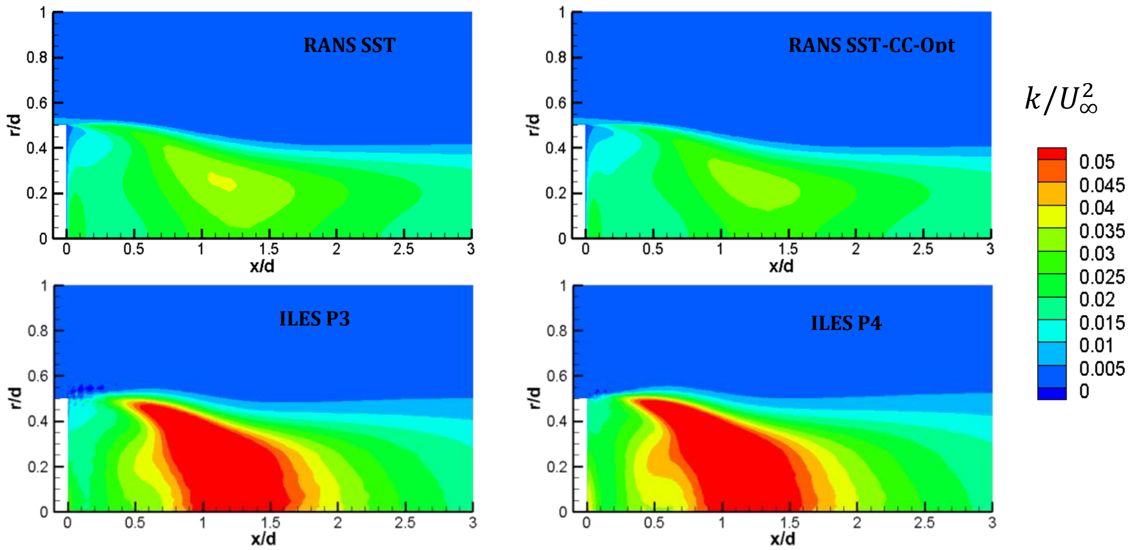

Figure 8: Comparison of turbulent kinetic energy, non-dimesionalized by square of free-stream velocity.

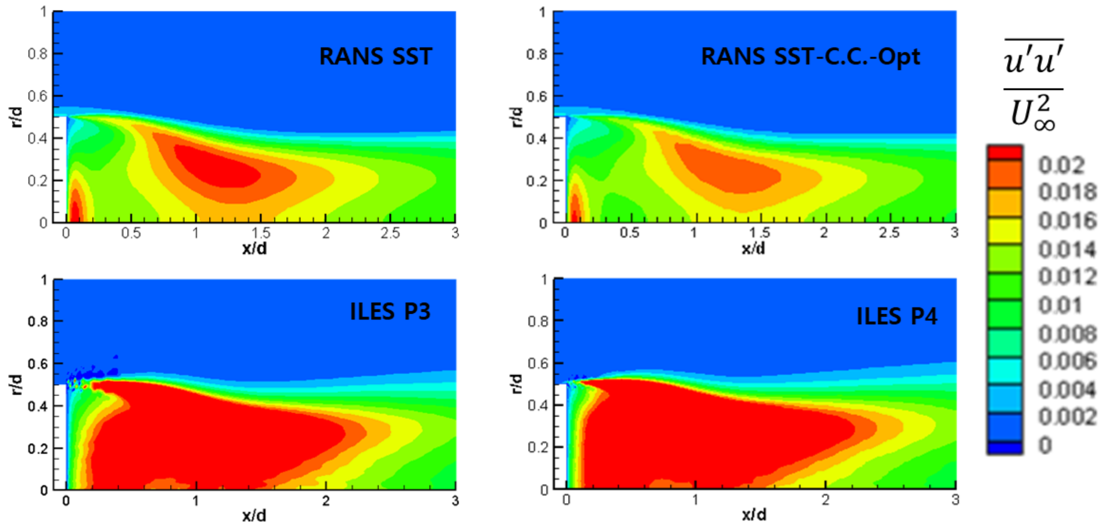

Figure 9: Comparison of Reynolds stress $\overline{u'u'}$

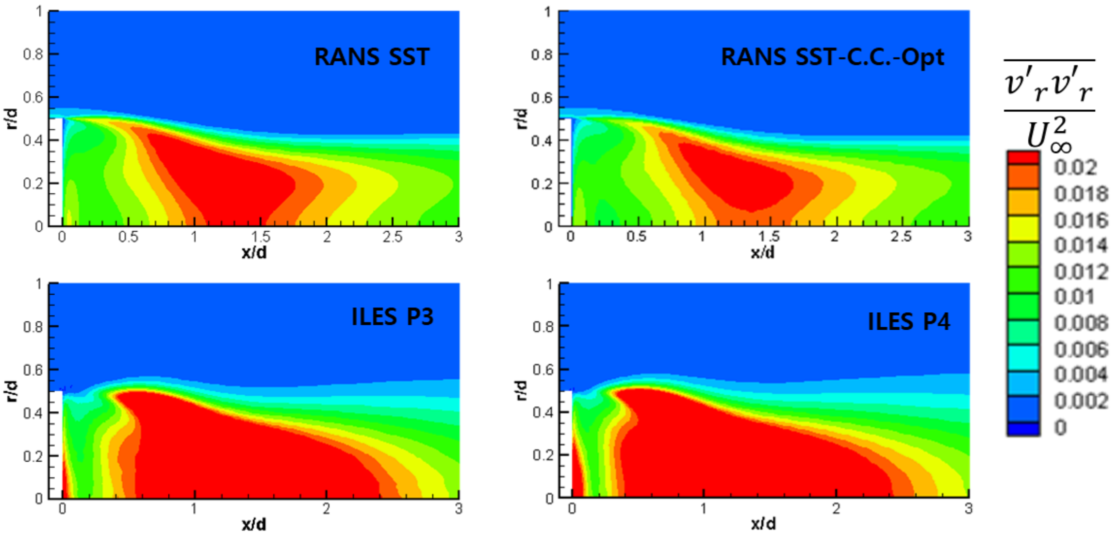

Figure 10: Comparison of Reynolds stress $\overline{\boldsymbol{v'_r v'_r}}$

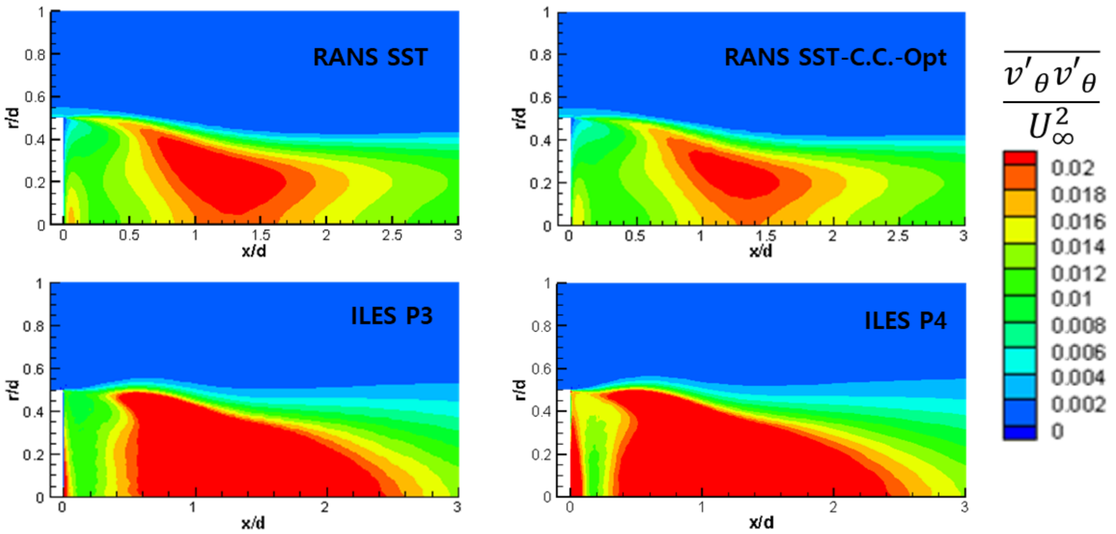

Figure 11: Comparison of Reynolds stress $\overline{\boldsymbol{v'_\theta v'_\theta}}$

The Reynolds stress tensor was also compared between RANS results and ILES results. Since the SST turbulence model approximates the Reynolds stress tensor using the eddy viscosity concept, it can be computed as follows:

$$-\overline{u'_i u'_j} = \nu_t \bar{S}_{ij} - \frac{2}{3} k \delta_{ij},$$

where $\overline{u'_i u'_j}$ denotes the ensemble-averaged Reynolds stress tensor, ν_t is the turbulent kinetic viscosity calculated by the turbulent model, $\bar{S}_{ij}$ is the mean strain tensor derived from the mean velocity field.

The Reynolds stress for ILES results was converted into cylindrical coordinates and time- and space-averaged. Figure 9 compares the $\overline{u'u'}$, the average of square of axial velocity fluctuation, for RANS simulations and ILES. ILES provides significantly more $\overline{u'u'}$, especially around recirculation region than RANS simulation. RANS simulations exhibit higher $\overline{u'u'}$ just after base wall.

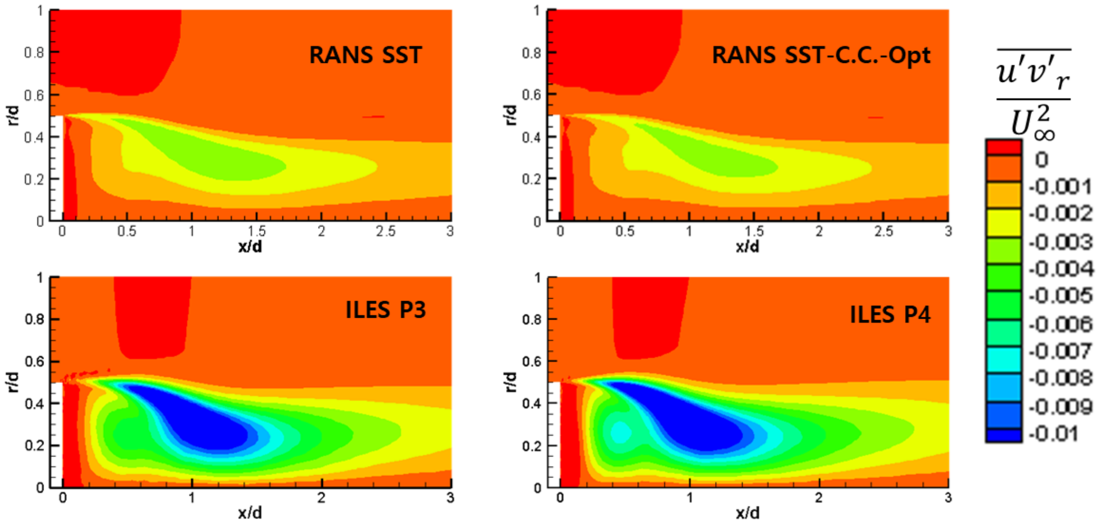

Figure 12: Comparison of Reynolds stress $\overline{\boldsymbol{u'v'_r}}$

Figure 10 compares $\overline{v'_r v'_r}$, the average of square of radial velocity fluctuation. Similar to $\overline{u'u'}$, ILES provides significantly higher stress around the recirculation region than RANS. Furthermore, ILES shows higher stress even just after the base wall, especially for the ILES P4 scheme. Figure 11 shows $\overline{v'_\theta v'_\theta}$, the average of square of azimuthal velocity fluctuation. The axisymmetric RANS simulation does not provide mean velocity strain rate, only provides $2/3k$. In addition, ILES shows a profile quite similar to $\overline{v'_r v'_r}$.

As well as comparison of normal Reynolds stress, the shear stress term $\overline{u'v'_r}$, the average of the average of the product of axial and radial velocity fluctuations was compared in Figure 12. ILES shows higher shear stress than RANS simulations, but the contour shape differs from that of the normal stress. It is also observed that ILES P4 provides more shear stress compared to other schemes.

This discrepancy in turbulent kinetic energy and Reynolds stress can be further explained by plotting instantaneous velocities obtained from ILES P4 simulations. Figures 13 and 14 show the instantaneous velocity components *v* and *w* at different time units. Unlike the mean velocity field shown in Figure 6, unsteady ILES simulations reveal small-scale vortical structures and their evolution. These vortical structures contribute to different turbulent characteristics, resulting in a shorter recirculation region and lower base pressure.

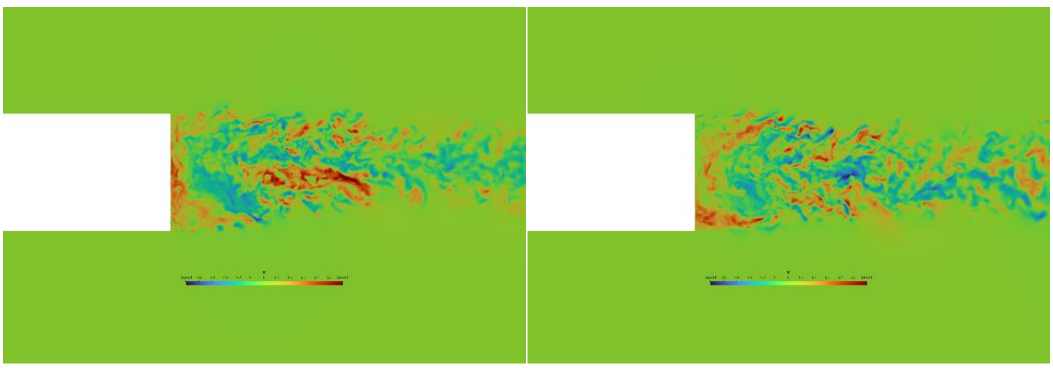

Figure 13: Instantaneous y-direction velocity contour for different time (Left : $t^* = 533.0$, Right: $t^* = 538.0$)

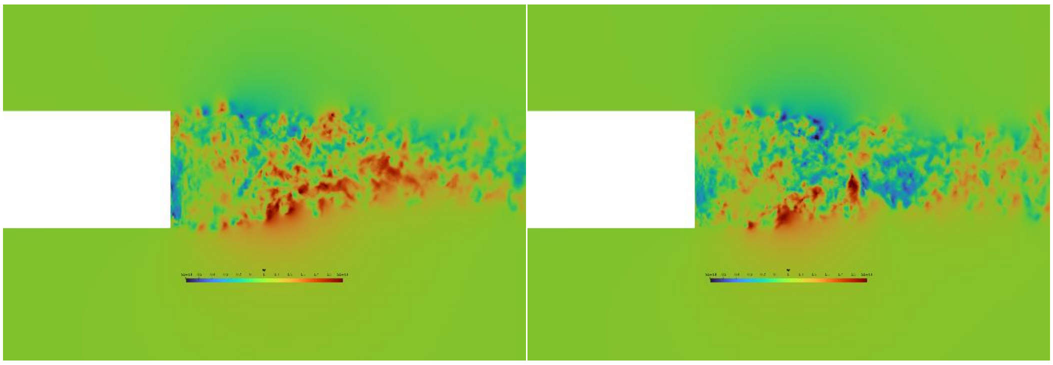

Figure 14: Instantaneous z directional velocity contour for different time (Left : $t^* = 533.0$, Right: $t^* = 538.0$)

4 Discussion

4.1 Relation Between Base Pressure and Recirculation Length

Marriotti et al. claimed a linear relationship between base pressure and recirculation length based on their experimental and numerical findings. To confirm this relationship, we plotted averaged base pressure coefficient C_{Pb} against the recirculation length l_r. The clear linear trend can be observed. As discussed, the behavior of small vortical structures influences the turbulent characteristics of the recirculation region, which supports this observed relationship.

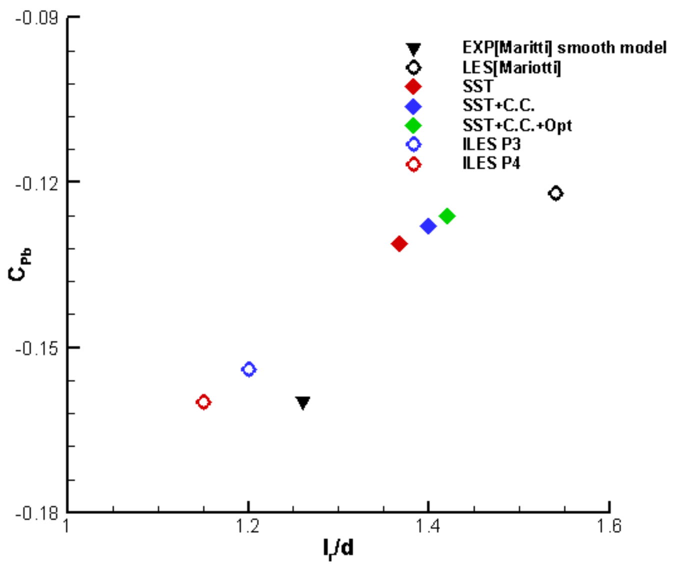

Figure 15: Relation between recirculation length and base pressure

4.2 Effect of Upstream Boundary Layer Thickness

It is hypothesized that the boundary layer thickness of upstream flow may influence downstream turbulent flow characteristics, including base pressure. To investigate this, we measured the velocity profile at a location upstream from the base edge at $x = -0.1d$ and calculated boundary layer thickness δ, as well as displacement thickness δ^* and momentum thickness θ. Figure 16 compares the velocity profile with other experimental and numerical results, and Table 3 summarizes these thicknesses along with the shape factor, which is the ratio of δ^* to θ.

ILES and VMS LES results show significantly shorter thicknesses compared to experimental results. In contrast, RANS results resemble the experimental data. Comparing the shape factor suggests that the upstream boundary layer flow in ILES and VMS LES simulations is laminar, whereas it appears turbulent in experiments and RANS simulations. Even experiments without a transition trip developed a turbulent boundary layer just before the base. ILES results maintain a laminar flow due to the absence of triggers such as free-stream turbulence or perturbations.

Despite these discrepancies in boundary layer flow characteristics, the base pressure predicted by ILES agrees well with experimental data. This suggests that the turbulent flow characteristics resulting from small vortical structures play a significant role in determining base pressure and the behavior of downstream separated flow rather than upstream boundary layer flow.

	δ/d	δ^*/d	θ/d	H
Exp Smooth[4]	0.107	0.0121	0.0086	1.41
Exp 1 strip[4]	0.143	0.0171	0.0121	1.41
Exp 2 strip[4]	0.171	0.0194	0.0144	1.35
VMS LES[4]	0.046	0.0146	0.0072	2.03
ILES P3	0.021	0.0096	0.0041	2.3606
ILES P4	0.021	0.0097	0.0041	2.3568
RANS SST	0.0707	0.0187	0.0126	1.4883
RANS SST-CC	0.0706	0.0187	0.0126	1.4900
RANS SST-CC-Opt	0.0704	0.0187	0.0126	1.4912

Table 1: Comparison between the boundary layer characteristics

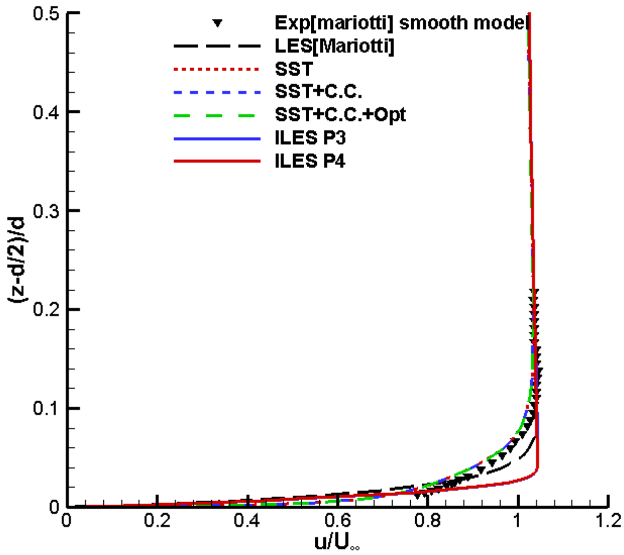

Figure 16: Velocity profile at x/d = -0.1

5 Conclusion

This study presented a comprehensive numerical investigation of subsonic flow over an axisymmetric blunt-based body using two turbulence modeling approaches: implicit large eddy simulations (ILES) with a high-order flux reconstruction scheme and Reynolds-averaged Navier-Stokes (RANS) simulations with a second-order finite volume method. Several flow structures were compared in relation to base pressure prediction. It was found that ILES provided significantly better predictions of the base pressure coefficient compared to RANS. By comparing the mean flow and turbulent flow characteristics, it became evident that accurately simulating the unsteady behavior of small-scale vortical structures has a significant impact on resolving highly separated base flow and predicting base pressure.

Acknowledgements

This work was supported by Data-driven Flow Modeling Research Laboratory funded by Defense Acquisition Program Administration under Grant UD230015SD, and National Supercomputing Center with supercomputing resources including technical support KSC-2022-CRE-038.

References

[1] Kim, D., Park, J., Park, J. S., and Lee, S. Optimized Ristorcelli's Compressibility Correction to the k-ω SST Turbulence Model for Base Flow Analysis. International Journal of Aeronautical and Space Sciences, 24(4), 1147-1159, 2023.

[2] Merz. R. A., Page. R. H. and Przirembel. CEG. Subsonic axisymmetric near-wake studies. AIAA J 16:656–662, 1978.

[3] Herrin. J. L. and Dutton. J. C. Supersonic base flow experiments in the near wake of a cylindrical afterbody. AIAA J 32:77–83, 1994.

[4] Kawai, S., and Fujii, K. Computational study of a supersonic base flow using hybrid turbulence methodology. AIAA journal, 43(6), 1265-1275, 2005.

[5] MARIOTTI, A. Experimental and numerical investigations for the characterization and control of separated flows. 2014.

[6] Shunn, L., and Ham, F. Symmetric quadrature rules for tetrahedra based on a cubic close-packed lattice arrangement. Journal of Computational and Applied Mathematics, 236(17), 4348-4364, 2012.

[7] Williams, D. M. *Energy stable high-order methods for simulating unsteady, viscous, compressible flows on unstructured grids*. Stanford University. 2013.

[8] Roe, P. L. Approximate Riemann solvers, parameter vectors, and difference schemes. Journal of computational physics, 43(2), 357-372, 1981.

[9] Cockburn, B., and Shu, C. W. The local discontinuous Galerkin method for time-dependent convection-diffusion systems. SIAM journal on numerical analysis, 35(6), 2440-2463, 1998.

[10] Kennedy, C. A., Carpenter, M. H., and Lewis, R. M. Low-storage, explicit Runge–Kutta schemes for the compressible Navier–Stokes equations. Applied numerical mathematics, 35(3), 177-219, 2000.

[11] Hairer, E., Wanner, G., and Solving, O. *II: Stiff and Differential-Algebraic Problems.* Berlin [etc.]: Springer. 1991.

[12] Van Leer, B. Towards the ultimate conservative difference scheme. Journal of computational physics, 135(2), 229-248, 1997.

[13] Beam, R. M., and Warming, R. F. Implicit numerical methods for the compressible Navier-Stokes and Euler equations. In Von Karman Inst. for Fluid Dyn. Computational Fluid Dyn. 99 p (SEE N83-19024 09-34, 1982.